Supporting Information

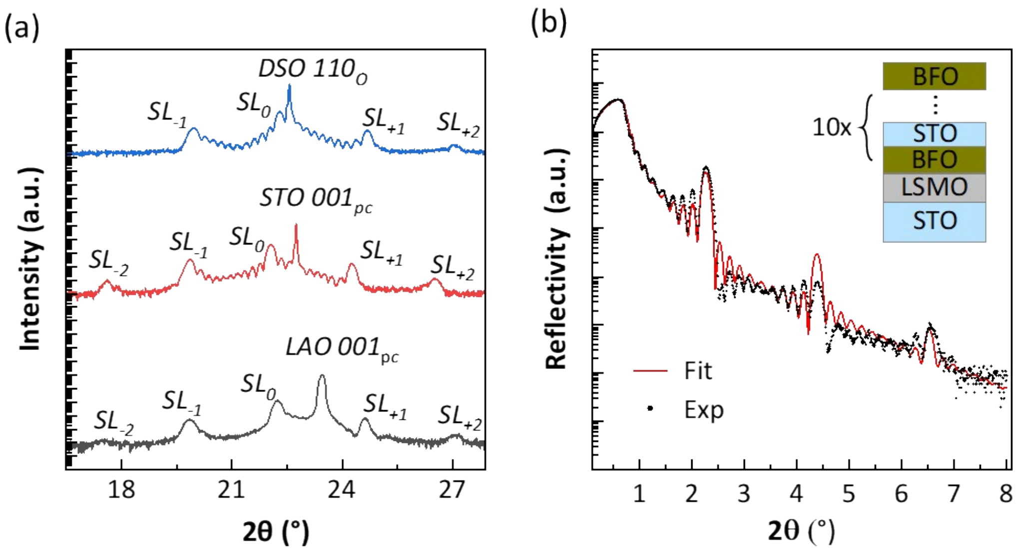

Figure S1. X-ray characterization of $(BFO)_7/(STO)_4$ superlattices grown on different substrate (a) coupled $2\theta - \omega$ scan about the 1st order reflection of the substrate, showing high-quality growth of the superlattices on all substrates (b) fitting of X-ray reflectometry pattern of representative $(BFO)_7/(STO)_4$ superlattice grown on LSMO-buffed STO(001) substrate. The excellent fit of the modelled structure ascertains the nominal thickness of each layer.

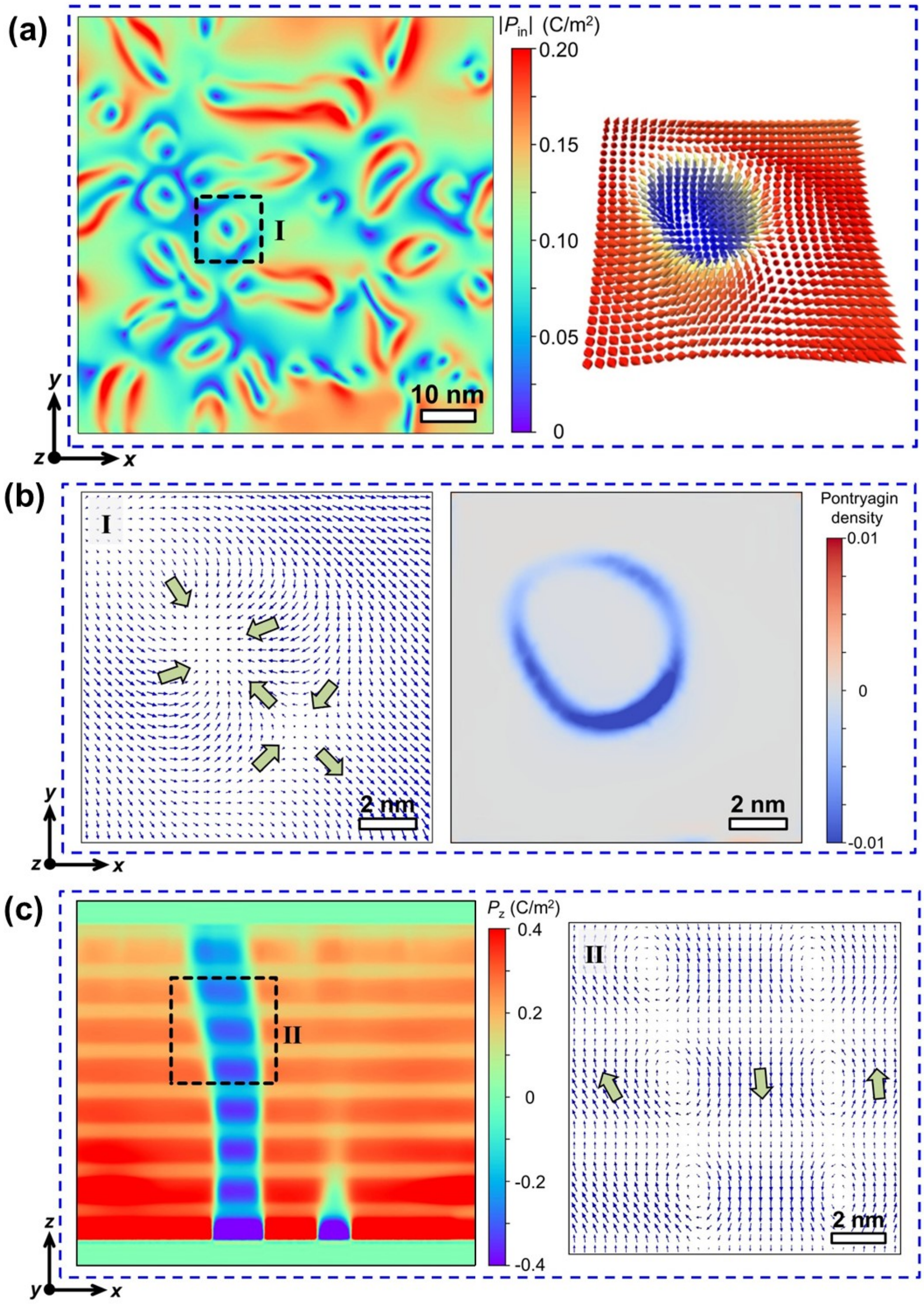

Figure S2. Polar structures and topological features of ferroelectric solitons in $(BFO_7/STO_4)_{10}$ superlattice system. (a) Planar view of polar solitons and its 3D illustration from the phase-field simulations. (b) Planar-view polarization and topological density distributions of single polar soliton marked with the black box I in (a), from the phase-field simulations. (c) Cross-sectional view of polar solitons and enlarged polarization distributions in the region II from the phase-field simulations.

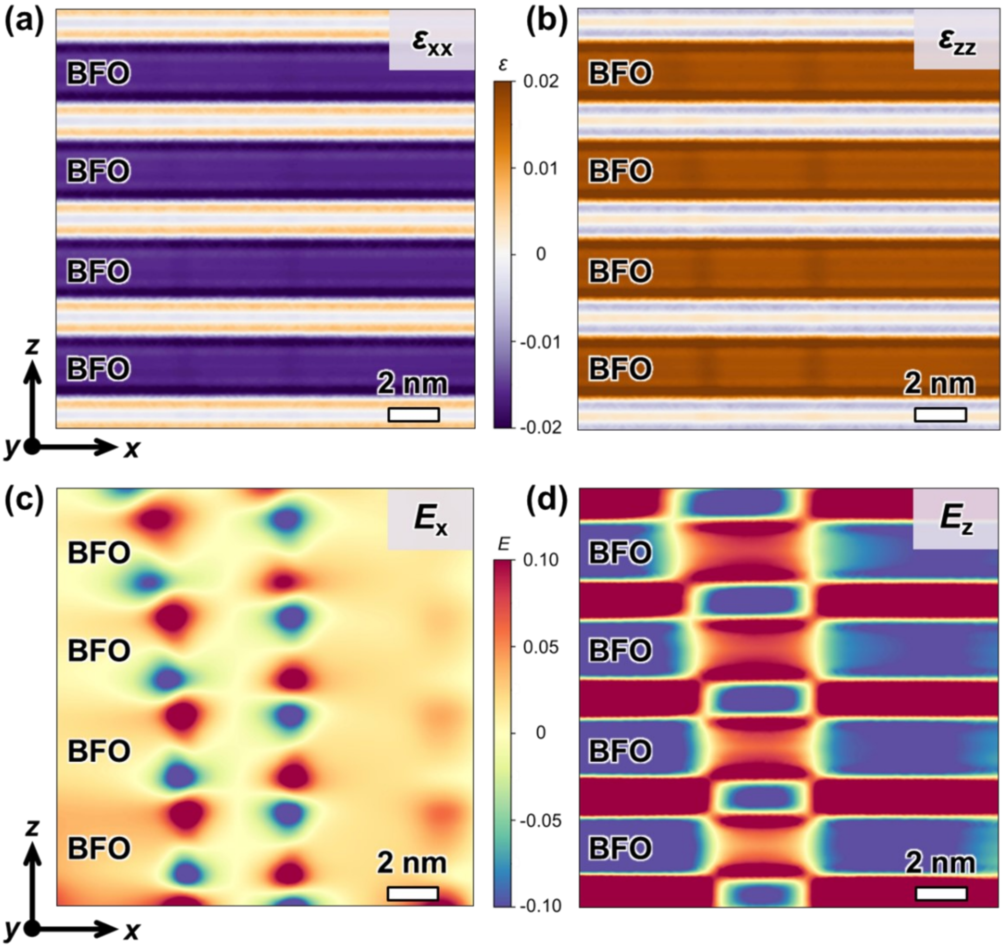

Figure S3. Analysis of local strain and electric field distribution of BFO_7/STO_4 superlattice grown on LAO substrate. (a) and (b) Cross-sectional view of the local strain ε_{xx} and ε_{zz} distribution for the BFO_7/STO_4 superlattice. (c) and (d) Cross-sectional view of the local electric field E_x and E_z distribution for the BFO_7/STO_4 superlattice.

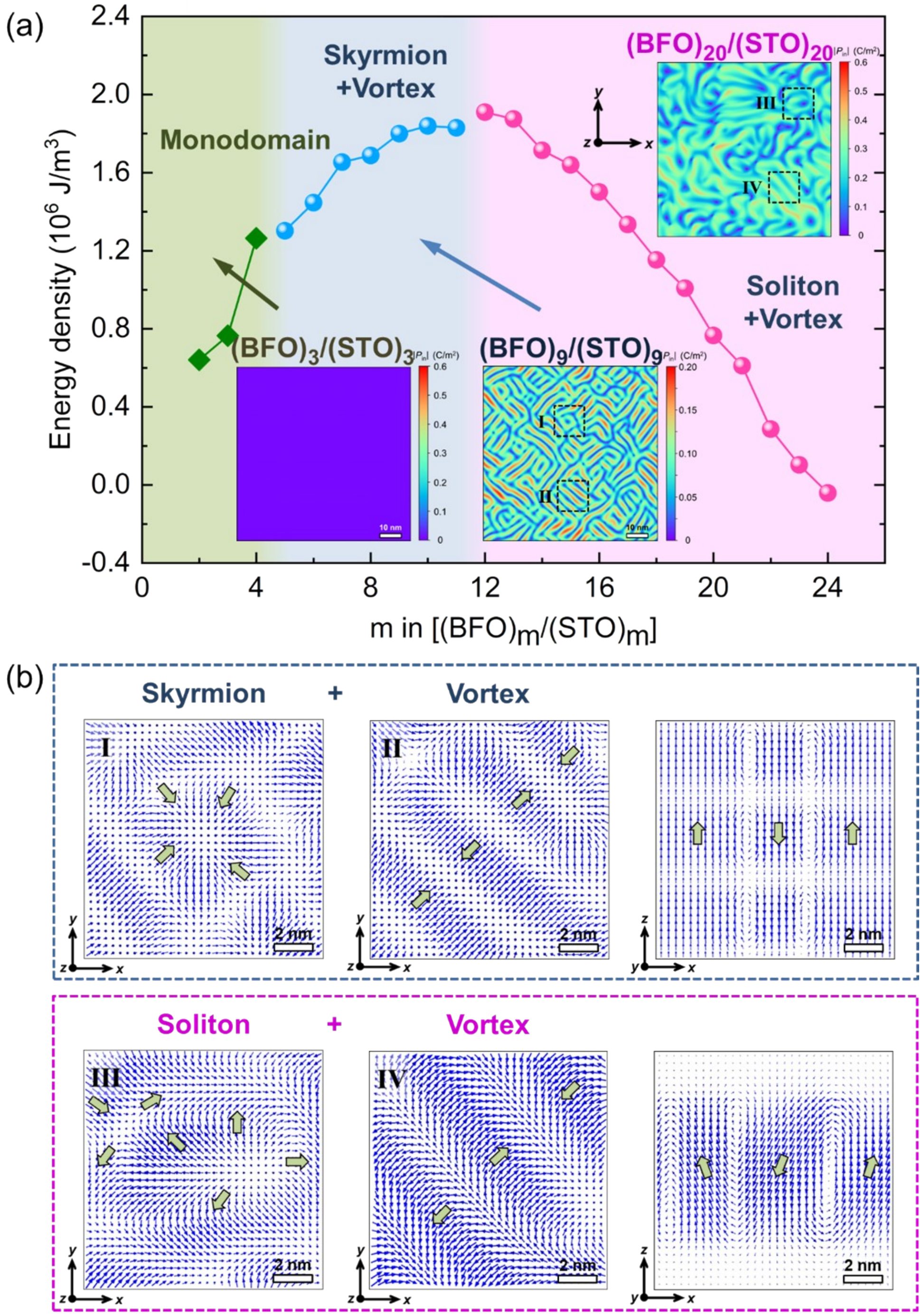

Figure S4. Film thickness phase diagram of polar topological defects in BFO_n/STO_n superlattice grown on LAO substrate. (a) Total energy density in BFO_n/STO_n systems as the function of the thickness n, calculated by phase-field simulations. (b) Planar view of mixture structure and enlarged cross-sectional view of its polarization distribution marked with the box I and II in the BFO_9/STO_9 superlattice and the box III and IV in the BFO_{20}/STO_{20} superlattice.

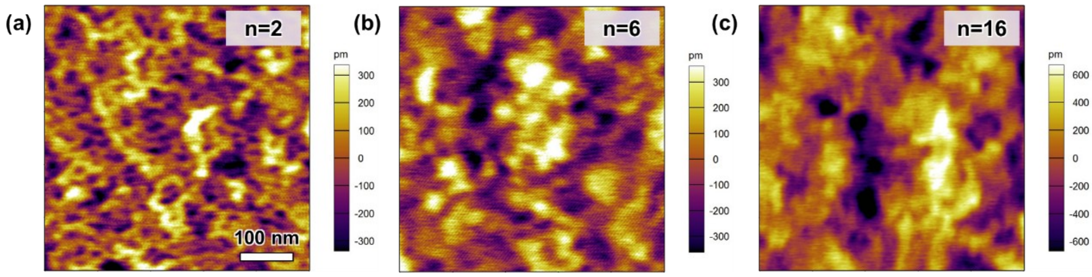

Figure S5. Topography image of BFO_n/STO_4 superlattices with varying layer thicknesses acquired by atomic force microscopy (a) BFO_2/STO_4, (b) BFO_6/STO_4, and (c) BFO_{16}/STO_4. Scale bars in (a-c) are 100 nm.

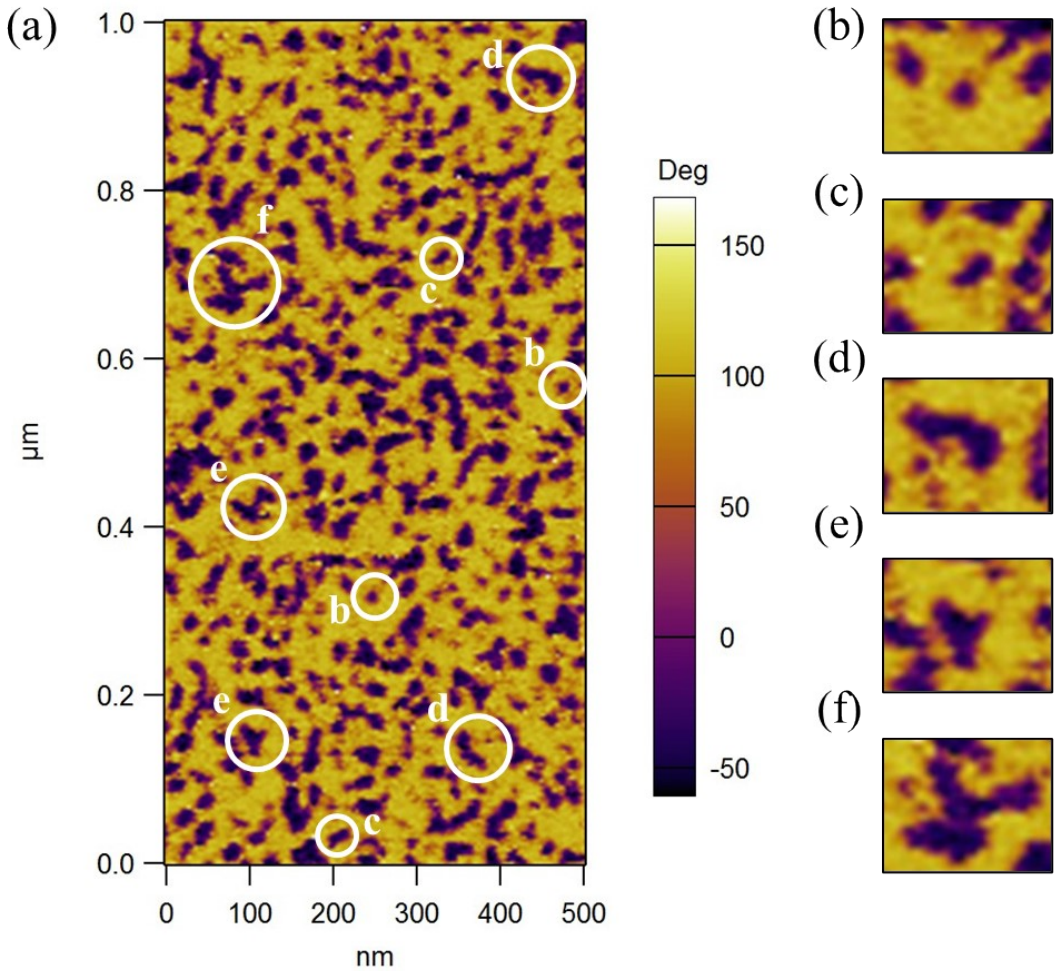

Figure S6. Transitional topological textures observed in BFO_6/STO_4 superlattice (a) PFM phase image showing various nontrivial polar states including (b) skyrmion (c) meron (d) bimeron (e) concave disclination and (f) fourfold junction

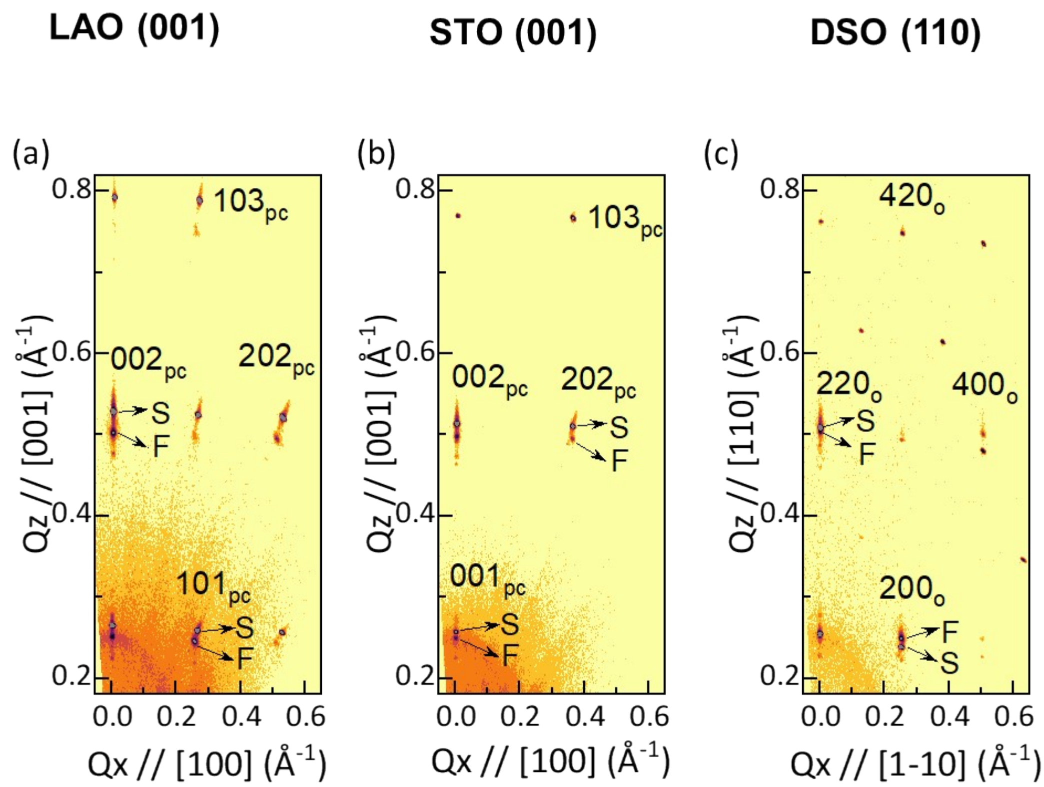

Figure S7. Wide two-dimensional reciprocal space maps of BFO_7/STO_4 superlattices grown on the different substrates. (a) (001) LAO, (b) (001) STO, and (c) (110) DSO substrates. It is noted that the average in-plane lattice parameter of $(BFO)_7/(STO)_4$ superlattice is in complete registry to that of STO and DSO substrate whilst it slightly relaxes when deposited on the LAO substrate due to the significant lattice mismatch between film and substrate.

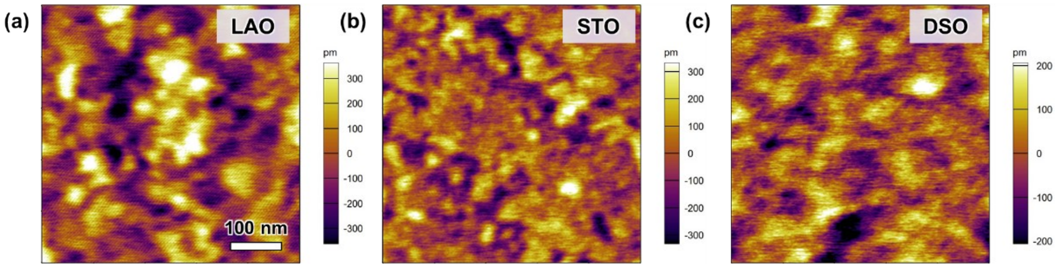

Figure S8. Topography image of BFO_7/STO_4 superlattices grown on the different substrates acquired by atomic force microscopy (a) LAO $(001)_{pc}$, (b) $STO(001)_c$, and (c) $DSO(110)_o$ substrates. Scale bars in (a-c) are 100 nm.

Table S1. Coefficients of $BiFeO_3$ used in the phase-field simulation

α_{11}	-3.580×10^{8} $C^{-2}\cdot m^{2}\cdot N$	κ_{1111}	7.840×10^{-11} $rad^{-2}\cdot N$
α_{1111}	3.000×10^{8} $C^{-4}\cdot m^{6}\cdot N$	κ_{1122}	-5.138×10^{-9} $rad^{-2}\cdot N$
α_{1122}	1.188×10^{8} $C^{-4}\cdot m^{6}\cdot N$	κ_{1212}	4.977×10^{-9} $rad^{-2}\cdot N$
β_{11}	-5.400×10^{9} $rad^{-2}\cdot m^{-2}\cdot N$	c_{1111}	2.280×10^{11} $N\cdot m^{-2}$
β_{1111}	3.440×10^{10} $rad^{-4}\cdot m^{-2}\cdot N$	c_{1122}	1.280×10^{11} $N\cdot m^{-2}$
β_{1122}	6.799×10^{10} $rad^{-4}\cdot m^{-2}\cdot N$	c_{1212}	0.650×10^{11} $N\cdot m^{-2}$
t_{1111}	4.532×10^{9} $C^{-2}\cdot rad^{-2}\cdot m^{2}\cdot N$	λ_{1111}	0.08416 rad^{-2}
t_{1122}	2.266×10^{9} $C^{-2}\cdot rad^{-2}\cdot m^{2}\cdot N$	λ_{1122}	-0.09200 rad^{-2}
t_{1212}	-4.840×10^{9} $C^{-2}\cdot rad^{-2}\cdot m^{2}\cdot N$	λ_{1212}	0.3192 rad^{-2}
g_{1111}	4.335×10^{-11} $C^{-2}\cdot m^{4}\cdot N$	h_{1111}	0.05700 $C^{-2}\cdot m^{4}$
g_{1122}	-3.400×10^{-12} $C^{-2}\cdot m^{4}\cdot N$	h_{1122}	-0.02000 $C^{-2}\cdot m^{4}$
g_{1212}	3.400×10^{-12} $C^{-2}\cdot m^{4}\cdot N$	h_{1212}	-0.0007300 $C^{-2}\cdot m^{4}$